A Detailed Physical Model for Ion Implant Induced Damage in Silicon

Shiyang Tian, *Member, IEEE*, Michael F. Morris, Steven J. Morris, Borna Obradovic, Geng Wang, Al F. Tasch, *Fellow, IEEE*, and Charles M. Snell

***Abstract*—A unified physically based ion implantation damage model has been developed which successfully predicts both the *impurity profiles* and the *damage profiles* for a wide range of implant conditions for arsenic, phosphorus, BF_2, and boron implants into single-crystal silicon. In addition, the *amorphous layer thicknesses* predicted by this new damage model are also in excellent agreement with experimental measurements. This damage model is based on the physics of point defects in silicon, and explicitly simulates the defect production, diffusion, and their interactions which include interstitial–vacancy recombination, clustering of same type of defects, defect–impurity complex formation, emission of mobile defects from clusters, and surface effects for the first time. New computationally efficient algorithms have been developed to overcome the barrier of the excessive computational requirements. In addition, the new model has been incorporated in the UT-MARLOWE ion implantation simulator, and has been developed primarily for use in engineering workstations. This damage model is the most physical model in the literature to date within the framework of the binary collision approximation (BCA), and provides the required, accurate as-implanted impurity profiles and damage profiles for transient enhanced diffusion (TED) simulation.**

***Index Terms*—Implant-induced damage, ion implantation, ion radiation effects, modeling, Monte Carlo methods.**

I. Introduction

ION implantation has been the dominant tool for introducing dopants into the silicon crystal for over two decades, and this trend is expected to continue well into the future. For example, a typical modern CMOS process employs approximately a dozen ion implant steps to form isolation wells, source/drains, channel-stops, threshold voltage adjusts, punchthrough stoppers, buried layers, and other doped areas of the p- and n-channel MOS transistors. During this process, the impurity ions are accelerated to kinetic energies ranging from a few keV to several MeV and are directed onto the surface of the semiconductor. As the ions enter the crystal, they give up their energy to the lattice atoms by means of electronic stopping and nuclear stopping, and they finally come to rest at some depth in the crystal. The energy loss of ions passing through matter can be divided into two components: nuclear stopping (energy loss to the medium's atomic positive cores) and electronic stopping (energy loss to the medium's light electrons). For Monte Carlo simulation, the nuclear stopping is treated with the binary collision approximation (BCA) [1], [2]. The energy of the ion is also lost to the electron cloud, which includes an inelastic loss during collisions which is due to the direct transfer of the electrons between the two colliding atoms, as well as an inelastic loss between collision which is due to the medium's polarization effect [3]. Finally, in order to simulate higher dose implants, a cumulative damage model is necessary. If the cumulative damage is not included, each projectile sees exactly the same crystal. Then two impurity profiles with different doses are scalable under identical conditions, i.e., the same energies, tilt angles, and rotation angles, etc. This is approximately true for low dose implants ($<10^{13}$ cm^{-2}) for which the probability for two damage regions overlapping is very small. However, at higher doses the shape of impurity profiles is largely altered as the dose increases. Therefore, a cumulative damage model is necessary in order to account for the dose dependence.

An obvious advantage of ion implantation is that it can be performed at room temperature; thus doping layers can be implanted without disturbing previously doped regions. Another major advantage of ion implantation is the precise control of the doping concentration and profiles. However, one of the major disadvantages of implantation is the lattice damage which results from the collisions between the energetic impurity ions and the lattice atoms. The other disadvantage is that a large fraction of the impurity atoms so introduced are in interstitial sites and thus are electrically inactive. In order to remove the damage and electrically activate the implanted impurities, it is necessary to introduce a subsequent thermal treatment called "annealing." Such a thermal annealing, however, can result in significant broadening of the dopant profiles due to diffusion.

Thus, the final doping profiles depend on both the initial as-implants profiles and the diffusion during the thermal cycles. Implantation damage dictates the final doping profiles in two ways.

1) The as-implanted profiles depend on the damage due to the damage dechanneling effect.
2) The damage generated during implants is the major source for transient enhanced diffusion (TED) during the subsequent thermal treatment [4].

Therefore, in order to obtain the final doping profiles after thermal processing, it is necessary to know not only the as-

Manuscript received June 9, 1997; revised October 10, 1997. The review of this paper was arranged by Editor A. H. Marshak. This work was supported in part by SRC, SEMATECH, Texas Advanced Technology Program, Eaton, Motorola, Intel, AMD, Micron, SGS Thomson, and Texas Instruments.

S. Tian was with the Microelectronics Research Center, University of Texas at Austin, Austin, TX 78712 USA. He is now with Avant! TCAD Business Unit, Fremont, CA 94538 USA.

M. F. Morris, S. J. Morris, B. Obradovic, G. Wang, and A. F. Tasch are with the Microelectronics Research Center, The University of Texas, Austin, TX 78712 USA.

C. M. Snell is with the Los Alamos National Lab, Los Alamos, NM 87545 USA.

Publisher Item Identifier S 0018-9383(98)03708-3.

implanted impurity profiles, but also the damage profiles. Thus, the modeling of the ion implantation damage process is motivated by two objectives. One is to simulate the defect dechanneling effect so that the impurity profiles as a function of dose can be accurately predicted. The other objective is to accurately predict the damage profiles so that these damage profiles can be used as inputs for transient enhanced diffusion (TED) simulation. Several simulators based on the binary collision approximation (BCA) have existed for years. In the BCA code, it is assumed that if the transferred energy exceeds a certain threshold (approximately 15 eV for implants into silicon), the target atoms are always displaced. It is assumed that at the lattice site where the target atom is displaced, a vacancy is generated. On the other hand, when the displaced atom comes to rest, it is identified as an interstitial. This very simplified picture is used in many Monte Carlo simulators [2], [5]–[8]. For example, Klein *et al.* [2] implemented a model by recording the final locations of all of the interstitials and vacancies for each ion cascade, and annihilating the interstitial–vacancy pairs which are within a specified capture radius. The recombination with the damage by previous cascades is accounted for by a statistical algorithm. Jaraíz *et al.* [8], [9] developed a more detailed model by keeping track of every interstitial and vacancy throughout the simulation, thus eliminating the statistical nature of the defect recombination algorithm. However, in their model single interstitials and vacancies are the only types of damage present and the interstitial–vacancy recombination is the only reaction process taking place during implantation. Thus, in order to reproduce the impurity profiles, a very small capture radius ($0.17a$, where a is the lattice constant) is used. However, such a small radius results in too much residual damage. In reality, much more complex defect structures, such as defect clusters, amorphous pockets, etc., are also formed. Ion irradiation can even lead to total amorphization of certain regions of the target crystal. Thus, it is not surprising to see that Jaraíz *et al.* [9] concluded that within this model impurity profiles and damage profiles cannot be accurately predicted at the same time. It is clear that although these simulators can provide satisfactorily accurate impurity profiles, they fail to accurately predict the damage profiles due to the simplified, incomplete physical models. Therefore, the major goal of this work is to develop a BCA based ion implantation simulator which can predict **both** the impurity profiles and the damage profiles accurately at the same time. It should be noted that although there were previous reports [7], [10] which show reasonable agreement with experiments for both the impurity profiles and the amorphous layer thicknesses, both the accuracy and the extent of applicability achieved by our model are unprecedented.

II. Kinetic Accumulative Damage Model (KADM)

In this section, we present in detail a new physically based ion implantation damage model, which explicitly simulates the defect production and its subsequent evolution into the as-implanted experimentally observable impurity and damage profiles. The hallmark of this damage model is that it simulates defect diffusion and interactions/reactions at room temperature after each ion cascade, and treats the damage accumulation, amorphization, and their complementary dechanneling processes consistently for the first time. In the next section, we shall also see how we overcome the barrier of the excessive computational requirements of this damage model by developing new efficient algorithms based on the fundamental physical principles.

A. Basic Assumptions

We assume that the implant is performed at or near room temperature. At higher temperatures defect diffusion and interaction involve many more processes than that at room temperature, and can be best treated by a diffusion simulator. However, even at room temperature, shortly after the collision cascade, local regions which receive large amounts of energies can be heated up to high temperature and may even become molten zones in a very short period of time ($<$ps). Then the temperature drops very rapidly (quenching) on the order of 1 ps [11]. During this process, large numbers of defects can recombine, and disordered zones can be recrystallized. This collective motion of defects can be best modeled by molecular dynamics (MD) [11], and cannot be adequately modeled within the framework of the BCA. Therefore, we take this process into account only approximately by recombining the close interstitial–vacancy pairs, as is in Klein's model [2] and Jaraíz's model [9]. After this recombination, the information of surviving defects is recorded for subsequent diffusion and reaction simulation. The validity of this assumption can be, of course, ultimately tested by experiments, and can also be judged from the quality of agreement between the simulation results and the experimental impurity and damage profiles. However, certain insight can be gained by examining this assumption in conjunction with the difference between the BCA and MD. Typically, MD produces much more damage initially than does the BCA. However, the quenching phase reduces this damage significantly, so that after the quenching phase MD and the BCA yield comparable amounts of damage. This is the primary reason why the BCA can also predict the damage profiles quite well, as will be demonstrated later, even though the quenching phase is taken into account only approximately. Thus, in our model, the damage process during ion implantation is divided into two phases: The first phase is defect production (displacement cascades), which takes place in less than 1 ps [12], while the second phase is defect diffusion and interaction, which happens shortly after the displacement cascade and lasts until the next ion comes to the same damage region. The second phase lasts for 0.1 ms or longer for typical dose rates.[1]

Under these basic assumptions, according to the migration energies of point defects, we can assume with confidence that only single vacancies and single interstitials are mobile at room temperature. The mobility of other defects at room temperature is much smaller because of their relatively higher

[1]The duration of the second phase can be estimated by using (3). For example, the diffusion time for each cascade is approximately 0.5 ms for a flux of 1 A/cm^2 and a $10a \times 10a$ (a is the silicon lattice constant) implant window.

migration energies [13]. We also assume that the vacancy migrates in the regular lattice sites, while the interstitial moves along a tetrahedral–hexagonal path. We further assume that all defect clusters are stable at room temperature because of their relatively large binding energies (>1 eV) [13]–[15]. Therefore, once defect clusters are formed, they cannot be dissociated by thermal energy at room temperature [13], [15]. However, as it will be shown later, defect clusters can become mobile through the annihilation of the opposite type of defect.

B. Defect Diffusion

The basic concept of the Monte Carlo diffusion simulation is the hopping frequency of a point defect from one equilibrium site to another in the crystal, and this can be computed following the jumping rate theory originally proposed by Vineyard [16]. With the harmonic approximation of the lattice vibrations, the hopping frequency can be expressed as follows:

$$\nu = \nu_0 e^{-E_m/k_B T} \tag{1}$$

where ν_0 is an effective attempt frequency ($\sim 10^{13}$ s^{-1} for silicon crystal [17]), E_m is the defect migration energy, k_B is Boltzmann's constant, and T is the substrate temperature. In our model, the migration energy for the vacancy is 0.45 eV, which was accurately determined by Watkins's experiments [18]. The interstitial migration energy ranges from 0.3 to 1.1 eV as calculated by *ab initio* and MD calculations in the literature [14], [19]. In our model, the migration energy for an interstitial is chosen to be 0.55 eV. It is interesting to relate the hopping frequency with the point defect diffusivity, which is typically given in the literature as a result of experimental diffusion measurements. According to random walk theory, the diffusion coefficient in every cubic-type lattice is given by

$$D = \tfrac{1}{6} d^2 \nu \tag{2}$$

where d is the jumping distance, i.e., the distance between two nearest-neighbor equilibrium sites. In diamond cubic lattices the nearest-neighbor distance is $d = (\sqrt{3}/4)a$, where a is the lattice constant. Combining (2) with (1) and using the migration energies given above, the diffusivity for vacancies is $D_V \approx 2 \times 10^{-11}$ cm^2/s, and the diffusivity for interstitials is $D_I \approx 5.5 \times 10^{-13}$ cm^2/s at room temperature.

In the new damage model, the mobile defects generated by ion cascades are allowed to diffuse for a certain amount of time. Roughly speaking, this diffusion time is determined by the dose rate (beam current) used during the implants. However, in order to determine the diffusion time after each ion cascade more precisely, both the beam current and the scanning pattern have to be taken into account. A detailed discussion of scanning pattern is outside of the scope of this paper, but interested readers are referred to [20]. In this paper, we shall employ a simple formula for diffusion time, which is valid for continuous exposure of wafers to the ion beam during implantation. However, for the scanning pattern of a given ion implanter, the time between successive ion cascades in the same local region can be derived. If we ignore the scanning pattern, the average diffusion time Δt is simply the reciprocal of the number of ions implanted into the implant window per second

$$\Delta t = \frac{1}{\text{const} \times \text{flux} \times (\text{window area})} \tag{3}$$

where const $= 6.25 \times 10^{18}$ is the number of charges per Coulomb, flux is the average flux in units of A/cm^2, and (window area) is the area of the implant window in units of cm^2. The concept of the implant window will be discussed in the next section.

C. Defect Interactions

In our model, defect interactions include interstitial–vacancy recombination, clustering of the same type of defects, defect–impurity complex formation, emission of mobile defects from clusters, and surface effects, etc. The details of these reactions are given next. The concept of the reaction radii for defects is introduced in this work because of the need to accommodate defect clusters. In our model, each defect has an inherent reaction radius. For single interstitials and single vacancies, this reaction radius is defined as a constant r_0. For a larger defect cluster with a defect number of n, the reaction radius is defined as $r = \sqrt[3]{n}\, r_0$. By this definition, we imply that the defects are approximately spherically distributed in a defect cluster. In our model, we assume that $r_0 = 0.4a$ for both single vacancy and single interstitial. Therefore, if one interstitial and one vacancy are separated as far as $0.4a + 0.4a = 0.8a$, they can recombine. Similarly, if two single point defects of the same type (single interstitial, single vacancy, dopant, etc.) are separated by $0.8a$, they can cluster to form di-interstitials, di-vacancies, or impurity clusters, etc. Larger defect clusters can be formed in the same manner. The "capture radius" of $0.8a$ is consistent with recent experimental data [21], which set the limit of the vacancy-interstitial recombination radius to be 10 Å, and the vacancy-boron recombination radius to be 5 Å.

Defect reactions can be formulated mathematically by using kinetic equations. The interaction/reaction rules given below are derived from the basic assumptions discussed at the beginning of this section.

1) Defect Recombination: Opposite types of defects can recombine to anneal out the damage.

$$I + V^n \rightarrow V^{n-1}$$
$$V + I^n \rightarrow I^{n-1}$$

Special cases:

$$I + V^2 \rightarrow V \qquad \text{(release a mobile vacancy)}$$
$$V + I^2 \rightarrow I \qquad \text{(release a mobile interstitial)}$$

Special case:

$$I + V \rightarrow 0 \qquad \text{(both vacancy and interstitial are annihilated).}$$

2) Defect Clustering: Same type of defects can cluster to form larger clusters.

$$I^n + I^m \rightarrow I^{n+m} \qquad \text{(interstitial clustering)}$$

Special case:

$$I + I \rightarrow I^2 \qquad \text{(di-interstitial formation)}$$
$$V^n + V^m \rightarrow V^{n+m} \qquad \text{(vacancy clustering)}$$

Special case:

$$V + V \rightarrow V^2 \qquad \text{(divacancy formation).}$$

3) Defect Complex Formation: Mobile defects can be trapped by impurity atoms and their complexes.

$$I + I^n A \rightarrow I^{n+1} A \qquad \text{(complex interaction)}$$
$$V + I^n A \rightarrow I^{n-1} A \qquad \text{(complex interaction)}$$
$$V + V^n A \rightarrow V^{n+1} A \qquad \text{(complex interaction)}$$
$$I + V^n A \rightarrow V^{n-1} A \qquad \text{(complex interaction)}$$

A: dopant, carbon, oxygen, etc.

4) Surface Recombination: Surface is assumed to be an effective sink for mobile defects.

$$I + \text{surface} \rightarrow \text{surface} \qquad \text{(surface recombination)}$$
$$V + \text{surface} \rightarrow \text{surface} \qquad \text{(surface recombination).}$$

D. Crystal Amorphization and Amorphous Pockets

It is well known that the amorphous pockets generated by high mass ion implants, as shown by MD calculations [11], cannot be well represented within the framework of the BCA and Monte Carlo techniques. In addition, the amorphization that occurs for implantation with low mass ions such as boron is believed to happen homogeneously when the interstitial concentration reaches a critical threshold [22]. In our damage model, the amorphous pockets and amorphous zones are modeled phenomenologically in two ways. First, the whole silicon crystal is divided into many small three-dimensional simulation cells. If the point defect concentration reaches a critical concentration in a particular cell, then this cell is locally amorphized. After amorphization, the defect diffusion and reaction rules described in the previous sections do not apply in this local region. The critical defect density for amorphization is taken to be 10% of the lattice atom density in the present model for all implant species [23]. It should be noted that in the literature the critical deposit energy density was used to determine the crystalline/amorphous transition [24], [25]. However, in their models the deposit energy accumulates linearly, and the critical densities vary from species to species due to different self-annealing characteristics [24]. In our approach, since self-annealing is taken into account explicitly, a single universal value is sufficient for all implant species. Second, the clustering has a higher priority to happen than recombination in a damaged region. Therefore, in a highly damaged region, the defects remain as "amorphous pockets" and would not completely anneal out due to random recombination. This preference is phenomenologically represented by an "amorphous pocket" formation probability P_a which is adjusted for each species to obtain the best agreement with experimental damage profiles. In the present model, $P_a = 0$ for boron implants, $P_a = 0.45$ for phosphorus and silicon implants, $P_a = 0.52$ for arsenic, and BF_2 implants.

E. Dechanneling Mechanisms

One consequence of the damage accumulation is its effect on the subsequently implanted ions. The damage can block the channel and change the destination of the subsequent ions, thus altering the shape of range profiles. Therefore, this is an essential part of damage modeling. In the present model, there are three possible dechanneling mechanisms. If a single interstitial is encountered, the interstitial is placed in a dumbbell configuration [26]. However, if an interstitial cluster is encountered, the defects are assumed to be randomly distributed within a sphere with radius equal to

$$r = \sqrt[3]{n}\, r_c \tag{4}$$

where n is the cluster size, and r_c is a constant. Finally, if an amorphous region is encountered, the projectile is assumed to travel in amorphous silicon until it is out of this region. It is noted that since the defect positions and other related information are recorded in this model, the dechanneling effect can be modeled much more rigorously than is possible by using only statistical approaches, as used in Posselt *et al.* [27] and Yang *et al.* [28]. It is also interesting to note that although the diffusion and reactions were treated with the same level of complexity, provisions were not made for this rigorously simulated damage to affect the trajectories of the subsequent ions (dechanneling) due to the complete separation of the cascade generation from the defect diffusion and reactions in the previous model [29]. Since dechanneling is so critical in determining the final impurity profiles, r_c was adjusted for each species. It was found that the same value of r_c can be used for arsenic, phosphorus, silicon, and BF_2 implants, but it is slightly less for boron implants. The possible reason for this is that higher mass implants generate much more highly disordered regions. These highly disordered zones can randomize the remaining regular lattice atoms, which effectively increases the collision radius r_c.

F. Model Summary

This damage model was originally proposed in [30]. The interaction/reaction rules are very similar to those of Beeler's RINGO [31] and Heinisch's ALSOME [32], which were applied only to implantation into metals. Our rules are also similar in many aspects to the kinetic Monte Carlo model developed independently by Jaraiz *et al.* [29], although their main interest is the high temperature defect diffusion and annealing simulation. It should be emphasized that despite this similarity in the diffusion and reaction simulation, our model is unique in treating the damage accumulation, amorphization, and the dechanneling processes consistently, e.g., moving ions are allowed to collide with defect clusters and amorphous pockets, as discussed in Sections II-D and II-E. This consistent treatment is essential in order for an ion implantation simulator to successfully predict both the impurity profiles and the damage profiles.

This damage model was developed as a universal model so that it can be applied to different implant species. Ideally, no species dependent parameters should be present in the model. However, due to the nature of modeling the damage as point

TABLE I
SUMMARY OF THE PARAMETERS USED IN KADM

Parameters	Implant Species				
	Arsenic	BF_2	Phosphorus	Silicon	Boron
Displacement Threshold E_d (eV)	15	15	15	15	15
Amorphization Threshold α (%)	10	10	10	10	10
Vacancy Migration Energy E_m^V (eV)	0.45	0.45	0.45	0.45	0.45
Interstitial Migration Energy E_m^I (eV)	0.55	0.55	0.55	0.55	0.55
Reaction Radius r_0 (Lattice Constant)	0.4	0.4	0.4	0.4	0.4
Collision Radius r_c (Lattice Constant)	0.24	0.24	0.24	0.24	0.20
Amorphous Pocket Probability P_a	0.52	0.52	0.4	0.4	0

defects in the BCA framework and its inadequacy of modeling amorphous pockets, some parameters must be adjusted in order to give the best overall agreement with experiments. It was found that in order to fit both the impurity and the damage profiles, as well as the amorphous layer thicknesses, two parameters (P_a and r_c) were required to be adjusted to obtain the best agreement with experiments. All other parameters are kept the same for all implants species. Most of the parameters used in this model are taken directly from reliable experimental data, *ab initio* calculations, or widely accepted values. A complete set of the parameters for our damage model are summarized in Table I. It can be seen that the difference between different implant species is very small, and values of the parameters vary in a consistent way. None of these parameters has unrealistic physical values. If molecular dynamics (MD) is the full dynamic simulation of the damage generation and evolution, this model is the kinetic counterpart of MD. Therefore, this damage model is referred to as kinetic accumulative damage model (KADM). We note in passing that in the literature, accumulative damage models are often referred to as dynamic damage accumulation [33]. The "dynamic" aspect refers to the way that the accumulated damage can dynamically dechannel the subsequent implanted ions. In this sense, our kinetic damage model is fully dynamic. Finally, this model has been integrated into UT-MARLOWE Version 4.0 [34] and has been very successfully applied to arsenic, phosphorus, silicon, BF_2, and boron implants. In order for this new model to be practical for use on engineering workstations, computationally efficient techniques were developed and incorporated in UT-MARLOWE. These are discussed next.

III. COMPUTATIONALLY EFFICIENT TECHNIQUES

In this section, two new approaches are discussed which improve the computational efficiency without compromising the basic physics and elements of the model. Ion implantation simulators have traditionally used a super-ion approach [2], [27], [28], in which each simulated ion represents a large part of dose. For example, if we use 3000 ions to simulate the implants at dose of 3×10^{13} cm^{-2}, then each simulated ion represents 10^{10} ions/cm^2. On the other hand, if we use 3000 ions to simulate 3×10^{15} dose implants, each ion represents 10^{12} ions/cm^2. Nonuniform weighting for each ion is also possible, and has been exploited to achieve the best statistics in the channeling tails for arsenic implants [28]. However, a question naturally arises: How valid is the assumption that one ion can represent a relatively large part of the dose? Since almost all of the physical properties used in the simulator are deduced from or calculated for single ions, such as interatomic potentials, electronic stopping powers, and even the binary collision formulas are derived based on the single particles, what is the relation between these single ions and the super-ions? This problem is particularly serious in the case of the damage simulation. For example, if we use the same 3000 ions to simulate the 3×10^{13} cm^{-2} and 3×10^{15} cm^{-2} implants, the number of point defects generated will be approximately the same except the weighting is different. This is clearly not physical. A more severe problem arises when using nonuniform weighting for each ion. For example, what happens if two different weighted defects recombine?

In order to avoid this ambiguity, in this work we propose a new approach which allows us to use one simulated ion to represent one real ion. The basic idea is to treat the ion implantation as implanting into an ensemble of implant windows and impose the periodic boundary conditions in the lateral direction for each implant window. Assuming that the ions are uniformly distributed across the wafer,[2] the number of ions implanted into each window can be easily found for a given dose as follows:

$$n = (\text{dose}) \times (\text{implant window}).$$

For example, for a $10 \times 10a^2$ window ($a = 5.43$ Å and is the lattice constant), $n \approx 3$, 30, 300, and 3000 for dose $= 10^{13}$, 10^{14}, 10^{15}, and 10^{16} cm^{-2}, respectively.[3] In principle, this is the number of ions required to do the simulation. More ions are used only to generate statistically significant profiles. Suppose that we want to use 3000 simulation ions. Then in order to simulate a dose of 10^{13} cm^{-2}, 1000 independent windows are required to finish the simulation with each window implanted with three ions. However, in order to simulate 10^{16} cm^{-2} implants, only one window is required into which all 3000 ions are implanted. Therefore, it is clear that a higher dose has more defect generation and interaction than does a lower dose, instead of just using simple weighting. The physical significance in this model is clearly evident, in contrast with the traditional super-ion approach. The implant window is chosen in such a way that its area is equal to or greater than the (average) damage area which is dependent on implant species and energy. That is, MeV implants should have a much larger window than keV implants. In practice, a $10 \times 10a^2$ window is sufficient for most keV implants.

This approach was termed "ion splitting" because of its splitting of the simulation ions into many different implant windows [35], and is in essence a "window mechanism." This approach has, in fact, more to do with physical reality than

[2] A statistical approach is also possible at the expense of extra CPU time.

[3] This number is only approximate in order to simplify the discussion.

with computational efficiency. However, for low dose implants, computational efficiency can be significantly improved for KADM because there are only three cascades interacting for a 10^{13} cm^{-2} dose for each implant window, rather than 3000 interacting cascades, as would be the case if a super-ion approach is used. Another advantage includes the ease with which the simulations can be run in parallel for low dose implants, because the different windows are independent. We next turn to a description of the ion shadowing approach.

Due to the fact that each ion cascade generates hundreds or even thousands of point defects, the number of ions required to generate the statistically significant damage profiles is much less than the number required to generate the impurity profiles. We can actually utilize this fact to advantage to reduce the CPU time considerably. The basic idea is to divide the simulation ions into "real" ions and "shadow" ions. The "real" ions generate full cascades, while the "shadow" ions are followed only as they travel through the damaged (by the "real" ions) crystal. The displaced silicon ions are not followed when the "shadow" ion is simulated, so that the computation time for the shadow ion is much less than that for the real ion. In practice, dependent on the implant species, the number of shadow ions associated with one real ion can be varied. This approach allows us to obtain both the impurity profiles and damage profiles with comparable statistical significance at the same time. This technique of reducing the computational time is referred to as "shadowing" [35].

One question which might arise is that if the shadow ions travel through the same damage region, do these ions stop at the same location? If so, they would not provide better statistics. Fortunately, in a Monte Carlo simulation, the initial positions are different from one ion to another, and also random factors such as lattice vibrations can contribute to the altering of the trajectories. Therefore, shadow ions will stop at different places according to the statistics even though the damage is the same. This situation is similar to that in which large ion numbers can be used to obtain statistic significance even though all of the simulated ions are implanted into virgin crystal, as is the case without damage accumulation. The combination of the ion shadowing and the window techniques presents a very powerful computational technique, and allows the very detailed damage model such as KADM to be simulated in a reasonable amount of CPU time on a typical workstation.

IV. Model Comparison with Experiments

In order to quantitatively validate this new damage model, we shall compare our simulation results including impurity profiles, damage profiles, and amorphous layer thicknesses with experimental data. Extensive comparisons have been made, and very good agreement has generally been obtained. In this section, we will show representative examples. Let us first briefly describe how we compare our simulation results with the SIMS impurity profiles, the RBS damage profiles, and the implant–induced amorphous layer thicknesses. The comparison with the SIMS profiles is straightforward, since both the simulation and the SIMS experiment give the chemical concentration of the implanted ions as a function of depth. However, the comparison with the RBS damage profiles requires more careful consideration. In general, the RBS backscattering yield from the channel direction is an indication of the lattice disorder [36]. Both interstitials and vacancies can contribute to the lattice disorder, although interstitials have a major contribution, because they not only distort the lattice, but also block the channels and directly backscatter the probing helium atoms [36]. The quantitative measure of the disorder is obtained by normalizing the RBS signals with respect to the reference spectrum which is obtained either from the random direction of crystalline silicon or from amorphous silicon [36]. In order to compare our simulation results to the RBS profiles, we assume that interstitials have the major contribution to the RBS yield. Therefore, we normalize the simulated interstitial profiles with respect to the amorphous concentration. To the first order of approximation, these normalized profiles should be comparable with the RBS damage profiles.

The amorphous/crystalline (a/c) interface depth can be obtained from the simulation results by examining the normalized interstitial profiles. In the figure of amorphization percentage versus depth, 100% of amorphization at a certain depth indicates that the crystal has been amorphized at that depth. However, the amorphous depth can sometimes be difficult to determine due to the statistical noise. In order to objectively and quantitatively determine the amorphous layer thicknesses, we use the following procedure. First, find the depth near the amorphous region at which the percentage of amorphization is decreasing most rapidly on a linear–linear plot. Next draw a line at this depth through the data and extrapolate this line to the top of the graph. The depth at which this extrapolated line reaches a value of 100% amorphization is our estimate of the a/c interface depth. This depth is equal to the amorphous layer thickness for samples with a surface amorphous layer. For buried amorphous layers, a similar procedure can be used to obtain the depth of the shallower crystalline/amorphous (c/a) interface. By subtracting the depths at which the c/a and a/c interface depths occur, the buried amorphous layer thickness can be obtained from a simulation. However, in order to compare with different experimental techniques, the extracted amorphous layer thicknesses for buried amorphous layers are estimated using the distance between the deeper a/c interface and the surface. The same procedure is also used to extract the amorphous layer thickness from the RBS profiles as well.

A. Arsenic Implants

Fig. 1 shows the comparison of the predicted impurity and damage profiles with the experimentally measured SIMS impurity profiles and the RBS damage profiles, respectively, for arsenic implants at an energy of 50 keV with two different tilt/rotation angles. The implant conditions are shown within the figure. It can be seen that the impurity profiles predicted by UT-MARLOWE with the new damage model (KADM) are in excellent agreement with the SIMS impurity profiles, and that the predicted damage profiles are in very good agreement with the RBS damage profiles. In particular, note that the crossover of the damage profiles at approximately

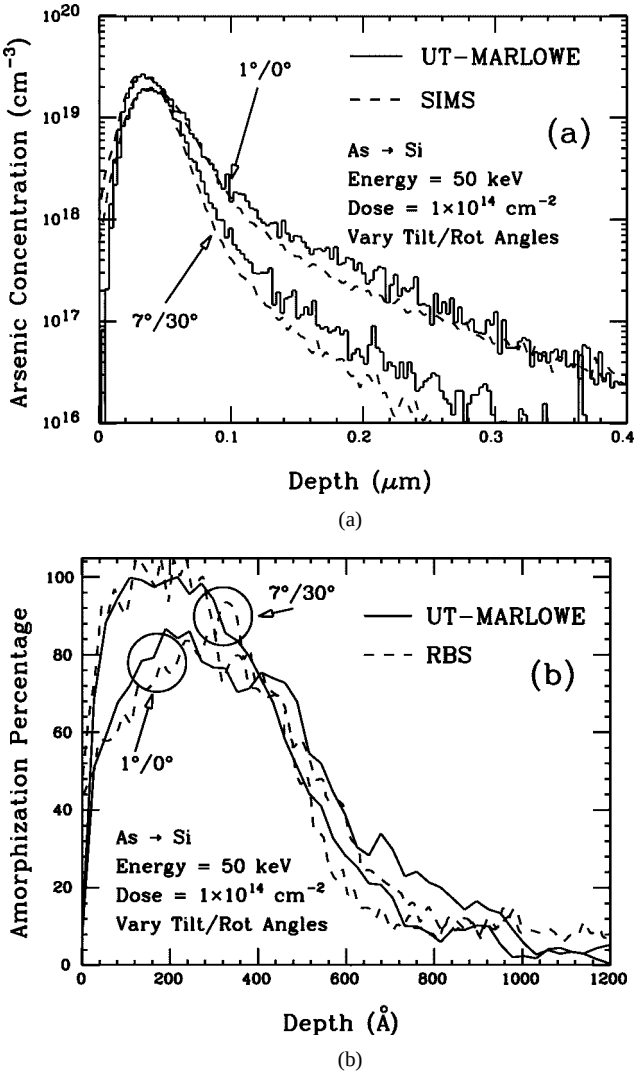

Fig. 1. Illustration of the ability of UT-MARLOWE with the new damage model (KADM) to accurately simulate the tilt/rotation angle dependence of both the impurity and the damage profiles for arsenic implants at an energy of 50 keV: (a) comparison with SIMS impurity profiles and (b) comparison with RBS damage profiles.

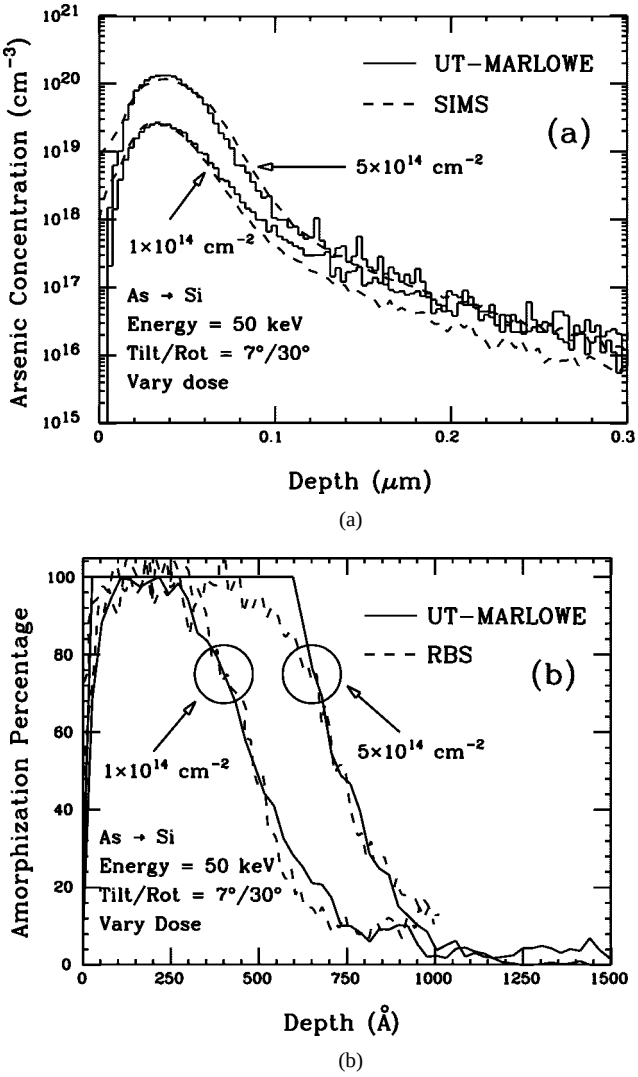

Fig. 2. Illustration of the ability of UT-MARLOWE with the new damage model (KADM) to accurately simulate the dose dependence of both the impurity and the damage profiles for arsenic implants at an energy of 50 keV: (a) comparison with SIMS impurity profiles and (b) comparison with RBS damage profiles.

450 Å is correctly predicted. Fig. 2 shows the comparison of the predicted impurity and damage profiles with experimental profiles for arsenic implants at the same energy of 50 keV, but with two different doses. It can be seen that UT-MARLOWE with the new damage model (KADM) predicts the dose dependence of both the impurity and the damage profiles excellently. For the 5×10^{14} cm^{-2} dose arsenic implant, the new damage model predicts an amorphous layer thickness of 600 Å, which is in good agreement with 650 Å determined by differential reflectometry measurement [37].

Our simulations suggest that the threshold dose for amorphization is insensitive to the implant ion energy in the energy range studied with higher energy having slightly higher threshold dose. This is consistent with experiment [38], and the threshold dose is predicted to be $\sim 10^{14}$ for arsenic implants in the energy range from 15 to 180 keV. Our simulations also suggest that below 180 keV, arsenic implants cannot produce a buried amorphous layer, which is also consistent with experiment [24].

Fig. 3(a) shows for arsenic implants the comparison of the predicted amorphous layer thicknesses with the experimental measurements including RBS, differential reflectometry, and XTEM. For any given sample, the various experimental measurements are generally in agreement, though differential reflectometry is found in general to have thicker amorphous layers than RBS. The agreement between the simulation results and the experiments is reasonably good, as can be seen in Fig. 3(a). It is interesting to point out that for the same dose, higher energy implants are predicted to have a thicker amorphous layer, and also for the same energy, higher dose implants have a thicker amorphous layer. This is in excellent agreement with experimental observations [24]. A quantitative relation between the amorphous layer thickness and the implant energy can also be obtained from these simulations. From Fig. 3(a) it is clear that for the same dose, the amorphous layer thickness is a linear function of implant energy in the energy range studied with higher doses having slightly steeper slopes. It is also noted that the

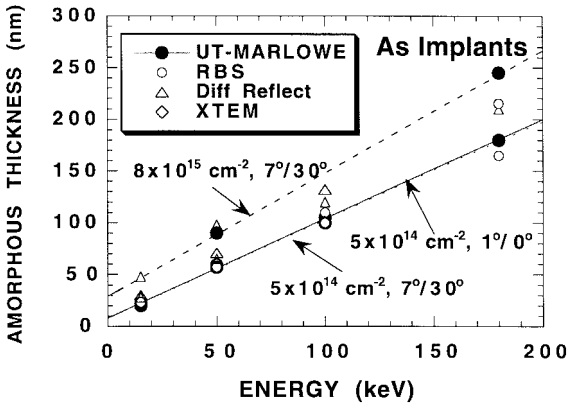

(a)

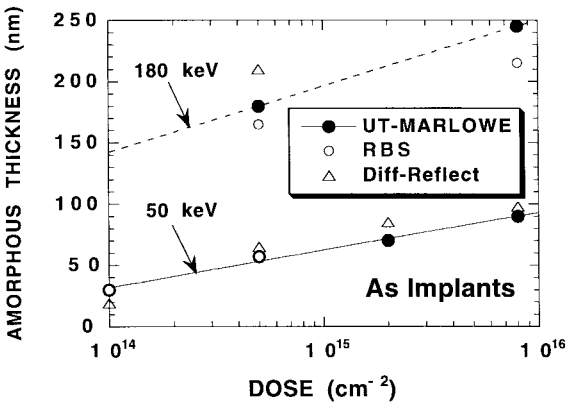

(b)

Fig. 3. Comparison of the predicted amorphous layer thicknesses with experimental measurements for arsenic implants as a function of (a) implant energy and (b) implant dose.

tilt/rotation angle has little effect on the amorphous layer thickness for arsenic implants. Mathematically, this relation can be expressed as follows:

$$t = aE + b \tag{6}$$

where t is the amorphous layer thickness in units of nm, E is the implant energy in units of keV, and a and b are constants for a given dose. For 5×10^{14} cm^{-2} implants, $a \approx 0.88$ nm/keV, and $b \approx 10$ nm. For 8×10^{15} cm^{-2} implants, $a \approx 1.2$ nm/keV, and $b \approx 30$ nm. This relation should be applicable from 10 to 200 keV. The same data can also be plotted as the amorphous layer thickness as a function of dose, as shown in Fig. 3(b). It can be seen that the amorphous layer thickness t is logarithmically dependent on the dose D ($D \geq 10^{14}$ cm^{-2}).

$$t = c \log D + d \tag{7}$$

where c and d are constants for a given energy. For 50 keV implants, $c \approx 51.6$ nm, and $d \approx -293$ nm. For 180 keV implants, $c \approx 101.6$ nm, and $d \approx -508$ nm.

B. Phosphorus Implants

Fig. 4 shows the tilt/rotation angle dependence of both the impurity and damage profiles for phosphorus implants into (100) Si at an energy of 80 keV and a dose of 5×10^{14} cm^{-2}. As can be seen, UT-MARLOWE with the new damage model (KADM) can predict the tilt/rotation angle dependence

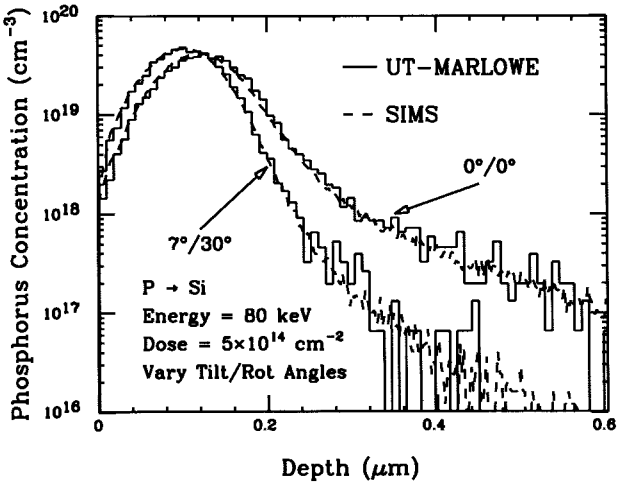

(a)

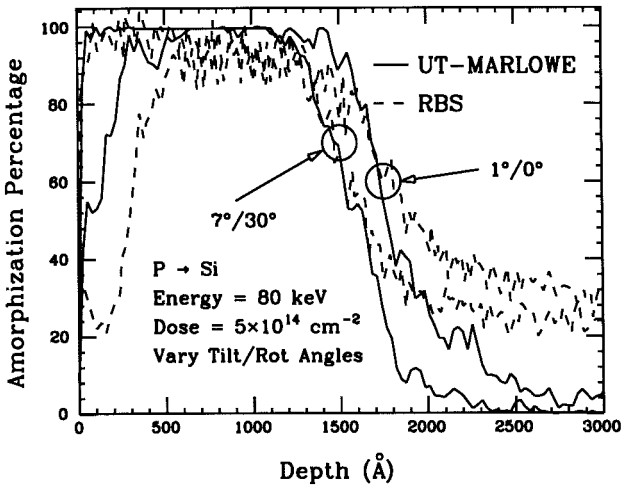

(b)

Fig. 4. Illustration of the ability of UT-MARLOWE with the new damage model (KADM) to accurately simulate the tilt/rotation angle dependence of both the impurity and the damage profiles for phosphorus implants at an energy of 80 keV and a dose of 5×10^{14} cm^{-2}: (a) comparison with SIMS impurity profiles and (b) comparison with RBS damage profiles. Note that the flat tails in the experimental RBS profiles are due to RBS background noise, and hence should be ignored.

of both the impurity and the damage profiles excellently. Fig. 5 shows the tilt/rotation angle dependence of both the impurity and damage profiles for phosphorus implants into (100) Si at an energy of 50 keV and a dose of 2×10^{15} cm^{-2}. Again, very good agreement is obtained between the simulations and the experimental results.

The amorphization threshold dose is predicted to be $\sim 3 \times 10^{14}$ cm^{-2} for phosphorus implants. For on-axis phosphorus implants, at energies above 80 keV, a buried amorphous layer can be formed. Both of these predictions are in very good agreement with experimental observations [24].

Fig. 6 compares the predicted amorphous layer thicknesses with RBS experimental data for phosphorus implants. The predicted amorphous layer thicknesses are in very good agreement with RBS experiments. Again, it is seen that for the same dose, higher energy implants have a thicker amorphous layer, and also for the same energy, higher dose implants have a thicker amorphous layer. The amorphous layer thickness can also be

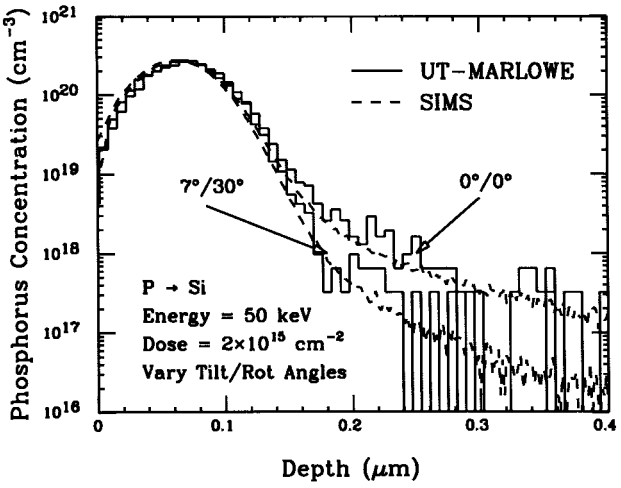

(a)

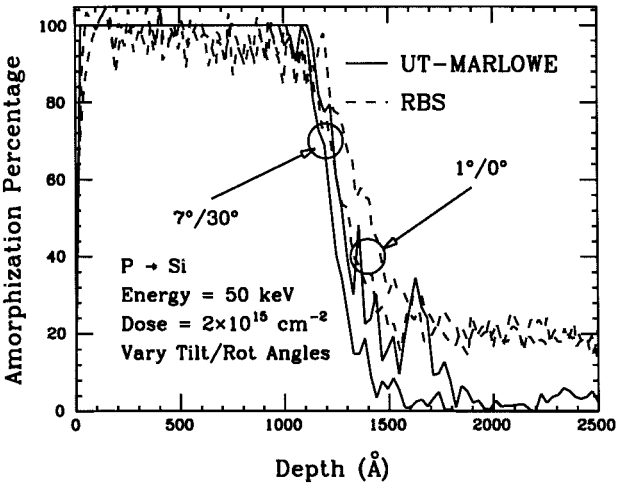

(b)

Fig. 5. Illustration of the ability of UT-MARLOWE with the new damage model (KADM) to accurately simulate the tilt/rotation angle dependence of both the impurity and the damage profiles for phosphorus implants at an energy of 50 keV and a dose of 2×10^{15} cm^{-2}: (a) comparison with SIMS impurity profiles and (b) comparison with RBS damage profiles. Note that the flat tails in the experimental RBS profiles are due to RBS background noise, and hence should be ignored.

well described by (6); however, for phosphorus implants at the same dose, 1° tilt implants produce a little thicker amorphous layer than do 7° tilt implants. The best fits to the data give $a \approx 1.6$ nm/keV, and $b \approx 10$ nm for 5×10^{14} cm^{-2}, 1°/0° implants; $a \approx 1.5$ nm/keV, and $b \approx 0$ nm for 5×10^{14} cm^{-2}, 7°/30° implants; $a \approx 1.78$ nm/keV, and $b \approx 27$ nm for 2×10^{15} cm^{-2}, 1°/0° implants; and $a \approx 1.71$ nm/keV, and $b \approx 19$ nm for 2×10^{15} cm^{-2}, 7°/30° implants.

C. BF_2 Implants

The molecular BF_2^+ ions are assumed to dissociate upon entry into the silicon substrate, since the bonding energy of boron and fluorine is approximately 10 eV, while the kinetic energy of the ions is two to three orders of magnitude larger than the bonding energy. The initial energies of boron and fluorine projectiles are given by $m_B/(m_B + 2m_F) \times E_0$ and $m_F/(m_B + 2m_F) \times E_0$, respectively, where E_0 is the implantation energy of BF_2^+ ions, and m_B and m_F are the

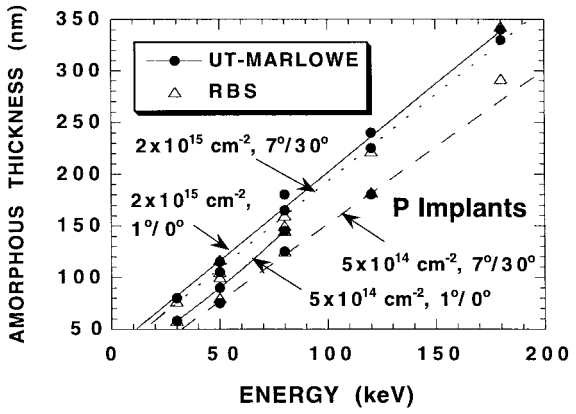

Fig. 6. Comparison of the predicted amorphous layer thicknesses with the experimental measurements for phosphorus implants.

atomic weights of boron and fluorine, respectively [39]. Fig. 7 shows the dose dependence of both the impurity and the damage profiles for BF_2 implants at an energy of 65 keV. The predicted impurity profiles and damage profiles are both in excellent agreement with the experimental data.

The amorphization threshold dose is also predicted to be $\sim 3 \times 10^{14}$ cm^{-2} for BF_2 implants. However, no buried amorphous layer can be seen for the energy range from 15 to 65 keV which we have studied.

Fig. 8(a) shows for BF_2 implants the comparison of the predicted amorphous layer thicknesses with experimental measurements (RBS and differential reflectometry). The agreement between the simulation results and the experiments is again very good. Again, it is seen that for the same dose, higher energy implants have a thicker amorphous layer, and also for the same energy higher dose implants have a thicker amorphous layer. As is the case with arsenic implants, the amorphous layer thickness is a linear function of the implant energy with higher doses having slightly steeper slopes. Also similar to arsenic implants, the tilt/rotation angle has little effect on the amorphous layer thickness for BF_2 implants. Quantitatively, (6) also applies for BF_2 implants with $a \approx 1.1$ nm/keV, and $b \approx 3.5$ nm for implants at a dose of 5×10^{14} cm^{-2}, and $a \approx 1.5$ nm/keV, and $b \approx 12.5$ nm for implants at a dose of 8×10^{15} cm^{-2}. The amorphous layer thickness can also be plotted as a function of dose, as shown in Fig. 8(b). Again, the amorphous layer thickness t is logarithmically dependent on the dose D ($D \geq 3 \times 10^{14}$ cm^{-2}), and can be described by (7). For 35 keV BF_2 implants, $c \approx 23.4$ nm, and $d \approx -139$ nm, and for 65 keV BF_2 implants, $c \approx 46.9$ nm, and $d \approx -243$ nm.

D. Boron Implants

Fig. 9 shows the predicted energy dependence of both the impurity and the damage profiles for boron implants at a dose of 8×10^{15} cm^{-2} and tilt/rotation angles of 1°/0°. The agreement with the SIMS profiles is excellent. Although the predicted amorphous layer thicknesses are approximately 30% thicker than the thicknesses inferred from the RBS measurements, they are in good agreement with the other experimental measurements, as will be shown below. Fig. 10(a) shows the dose dependence of the impurity profiles for off-axis (7°/30°) and 15 keV energy, and Fig. 10(b) shows the dose dependence

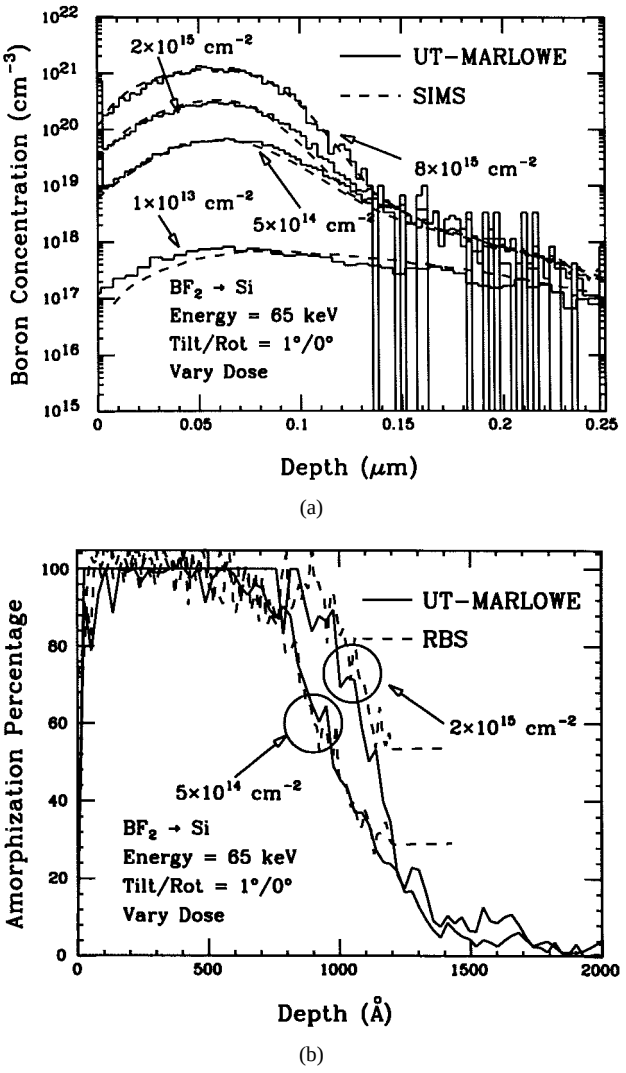

Fig. 7. Illustration of the ability of UT-MARLOWE with the new damage model (KADM) to accurately simulate the dose dependence of both the impurity and the damage profiles for BF_2 implants at an energy of 65 keV: (a) comparison with SIMS impurity profiles and (b) comparison with RBS damage profiles. Note that the new damage model also successfully predicts the amorphous layer thicknesses.

of the impurity profiles for on-axis (0°/0°) boron implants at an energy of 80 keV. Excellent agreement is obtained between the simulations and the experiments.

In the literature, the reported amorphization doses for boron implants range from 5×10^{15} cm^{-2} for high beam currents (50 μA/cm^2) [40] to 8×10^{16} cm^{-2} for low beam currents (0.2 μA/cm^2) [38] at room temperature. This difference is believed to be largely due to the dose rate effect. For the medium beam current implants (5-20 μA/cm^2) used in this study, for 8×10^{15} cm^{-2} boron implants, three different experimental techniques (RBS, TGP, and differential reflectometry) indicate that an amorphous layer is present. Our simulations suggest that the amorphization occurs for medium beam current boron implants at a dose of $\sim 7 \times 10^{15}$ cm^{-2}. A buried amorphous layer can be formed for on-axis boron implants at a relatively low energy ($\sim$40 keV).

Fig. 11 compares the amorphous layer thicknesses predicted by UT-MARLOWE with the results based on three different experimental techniques (including RBS, differential

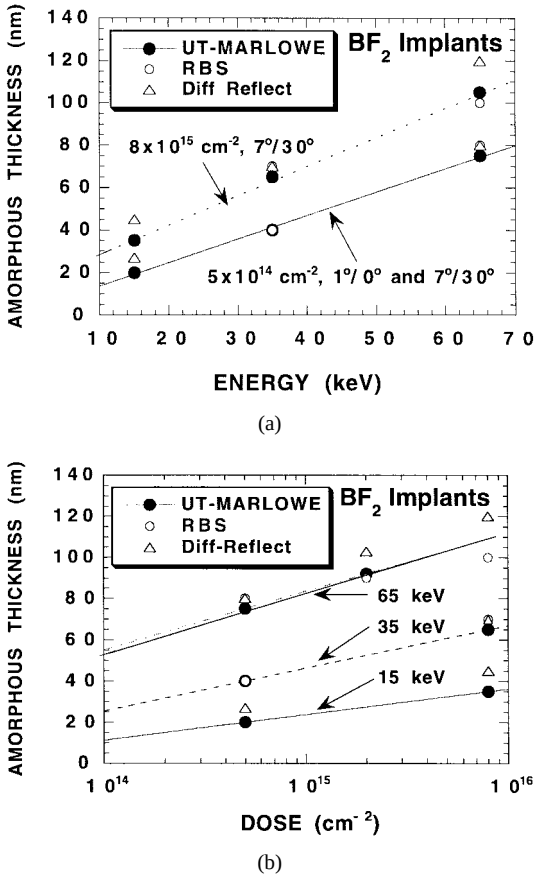

Fig. 8. Comparison of the predicted amorphous layer thicknesses with the experimental measurements for BF_2 implants as a function of (a) implant energy, and (b) implant dose.

reflectometry, and TGP [24]) for boron implants. From this figure, it is clear that substantial discrepancies exist among the different experimental techniques for the amorphous layer thicknesses induced by boron implants, and the amorphous layer thicknesses measured by RBS are in general thinner than those measured by other techniques. However, the simulation results fall in the middle of the scattered experimental data. Based on this fact, we believe that our model is reliable even though it is not in very good agreement with the RBS data for boron implants. Again, it is seen that for the same dose, higher energy implants have a thicker amorphous layer, and for the same dose 1° tilt implants have a thicker amorphous layer than do 7° implants. However, for boron implants, unlike other species the dependence of the amorphous layer thickness on the implant energy slightly deviates from a linear relationship.

V. Conclusions

A unified physically based ion implantation damage model (KADM) has been presented in detail in this paper. This damage model explicitly accounts for damage production, damage dechanneling, defect diffusion and reactions, and crystal amorphization at room temperature. The damage production and dechanneling are based on the binary collision approximation (BCA), and the defect diffusion and reactions are based on point defect kinetics and energetics in silicon. The defect diffusion is modeled by the Monte Carlo hopping algorithm, while the defect reactions include interstitial–vacancy

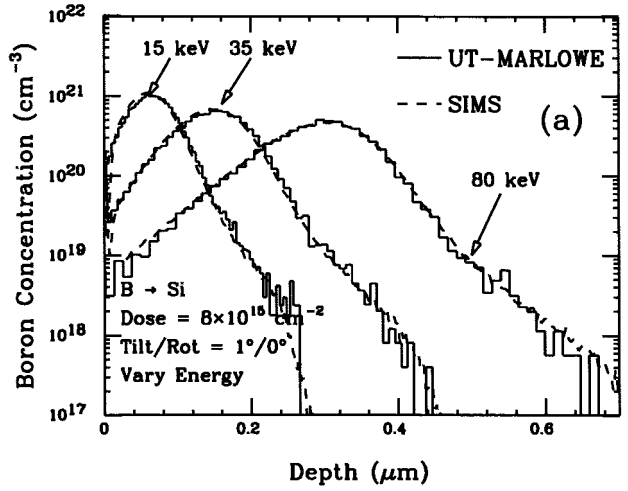

(a)

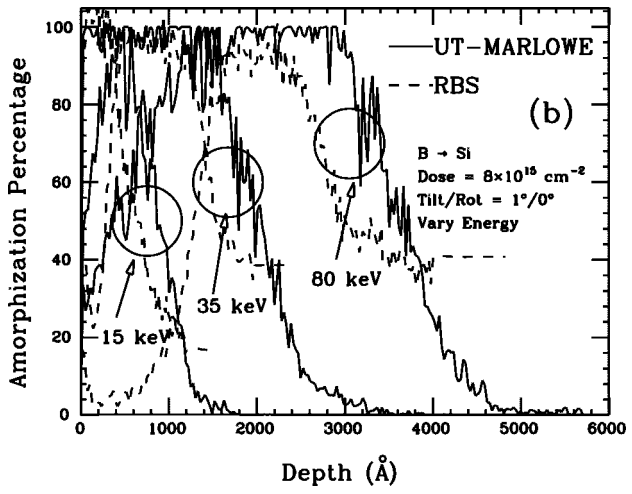

(b)

Fig. 9. Illustration of the ability of UT-MARLOWE with the new damage model (KADM) to accurately simulate the energy dependence of both the impurity and the damage profiles for boron implants at a tilt/rotation angle of $1^\circ/0^\circ$: (a) comparison with SIMS impurity profiles and (b) comparison with RBS damage profiles.

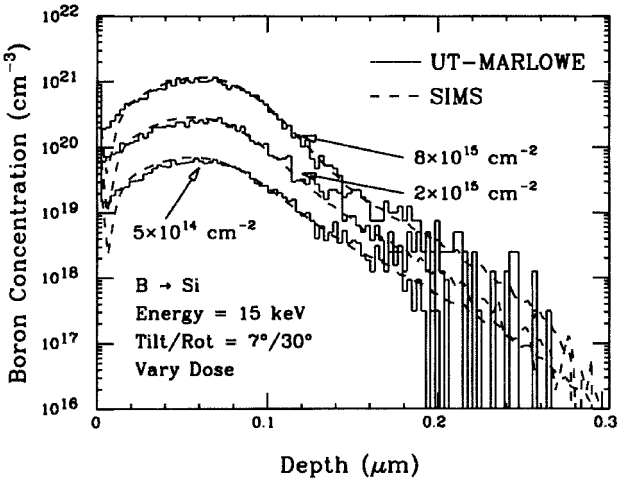

(a)

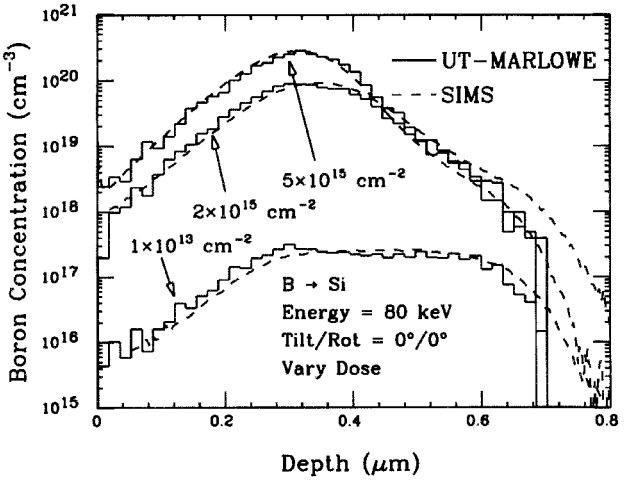

(b)

Fig. 10. Illustration of the ability of UT-MARLOWE with the new damage model (KADM) to accurately simulate the dose dependence of the impurity profiles for (a) off-axis ($7^\circ/30^\circ$) boron implants at an energy of 15 keV and (b) on-axis ($0^\circ/0^\circ$) boron implants at an energy of 80 keV.

recombination, clustering of same type of defects, defect-impurity complex formation, emission of mobile defects from clusters, and surface effects. New computationally efficient algorithms have been developed to overcome the barrier of excessive computational requirements.

This damage model simulates point defect diffusion and reactions at room temperature after each ion cascade, and treats the damage accumulation, amorphization, and the complementary dechanneling processes consistently for the first time, and is the most physical model in the literature to date within the framework of the binary collision approximation (BCA). This damage model has been successfully applied to arsenic, phosphorus, BF_2, and boron implants. The predicted *impurity profiles* and *damage profiles* are in excellent agreement with the SIMS impurity profiles and the RBS damage profiles, respectively, for a wide range of implant conditions for arsenic, phosphorus, BF_2, and boron implants. In addition, the *amorphous layer thicknesses* predicted by this damage model are also in very good agreement with experimental

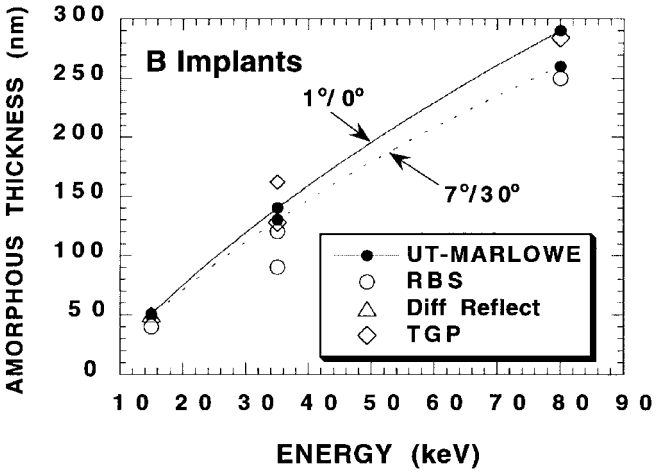

Fig. 11. Amorphous layer thickness as a function of energy for boron implants at a dose of 8×10^{15} cm^{-2}. The solid and dash curves are visual guides to the UT-MARLOWE simulation data points. Note that the simulation results fall in the middle of the scattered experimental data.

measurements. Thus, this damage model for the *first* time provides both the accurate as-implanted impurity profiles and accurate as-implanted damage profiles which are necessary for reliable transient enhanced diffusion (TED) simulation.

ACKNOWLEDGMENT

The authors would like to thank Dr. S. Baumann of Evans Texas for his RBS measurements, Dr. C. Magee and Dr. J. Sheng of Charles Evans for their SIMS measurements, Dr. R. Hummel of the University of Florida for his differential reflectometry measurements, and Dr. S. Prussin of UCLA for his TGP measurements.

REFERENCES

[1] M. T. Robinson and I. M. Torrens, "Computer simulation of atomic-displacement cascades in solids in the binary-collision approximation," *Phys. Rev. B,* vol. 9, pp. 5008–5024, June 1974.
[2] K. M. Klein, C. Park, and A. F. Tasch, "Monte Carlo simulation of boron implantation into single-crystal silicon," *IEEE Trans. Electron Devices,* vol. 39, pp. 1614–1621, July 1992.
[3] S. J. Morris, "Electronic stopping in single-crystal silicon from a few keV to several MeV," Ph.D. dissertation, Univ. Texas, Austin, May 1997.
[4] D. J. Eaglesham, P. A. Stolk, H.-J. Gossmann, and J. M. Poate, "Implantation and transient B diffusion in Si: The source of the interstitials," *Appl. Phys. Lett.,* vol. 65, pp. 2305–2307, Oct. 1994.
[5] J. Ziegler, J. Biersack, and U. Littmar, *The Stopping and Range of Ions in Solids.* New York: Pergamon, 1985.
[6] B. J. Mulvaney, W. B. Richardson, and T. L. Crandle, "PEPPER—A process simulator for VLSI," *IEEE Trans. Computer-Aided Design,* vol. 8, pp. 336–349, Apr. 1989.
[7] G. Hobler, "Net point defect concentrations after ion implantation in silicon," in *Proc. Electrochem. Soc.,* 1996, vol. 96-4, pp. 509–521.
[8] M. Jaraíz, J. Arias, J. E. Rubio, L. A. Bailón, and J. Barbolla, "Computer simulation of point-defect distributions generated by ion implantation," *Nucl. Instrum. Methods Phys. Res. B,* vols. 80/81, pp. 172–175, 1993.
[9] M. Jaraíz, J. Arias, L. A. Bailón, and J. Barbolla, "Detailed computer simulation of damage accumulation in ion irradiated crystalline targets," *Vacuum,* vol. 44, nos. 3/4, pp. 321–323, 1993.
[10] M. Posselt, B. Schmidt, C. S. Murthy, T. Feudel, and K. Suzuki, "Modeling of damage accumulation during ion implantation into single-crystalline silicon," *J. Electrochem. Soc.,* vol. 144, pp. 1495–1504, 1997.
[11] M.-J. Caturla, T. Diaz de la Rubia, L. A. Marqués, and G. H. Gilmer, "Ion beam processing of silicon at keV energies: A molecular dynamics study," *Phys. Rev. B,* vol. 54, pp. 16683–16695, Dec. 1996.
[12] O. S. Oen and M. T. Robinson, "Slowing-down time of energetic ions in solids," *J. Appl. Phys.,* vol. 46, pp. 5069–5071, Dec. 1975.
[13] G. D. Watkins and J. W. Corbett, "Defects in irradiated silicon: Electron paramagnetic resonance of the divacancy," *Phys. Rev.,* vol. 138, no. 2A, pp. A543–A555, 1965.
[14] G. H. Gilmer, T. Diaz de la Rubia, D. M. Stock, and M. Jaraiz, "Diffusion and interactions of point defects in silicon: Molecular dynamics simulations," *Nucl. Instrum. Methods Phys. Res. B,* vol. 102, pp. 247–255, 1995.
[15] E. G. Song, E. Kim, Y. H. Lee, and Y. G. Hwang, "Fully relaxed point defects in crystalline silicon," *Phys. Rev. B,* vol. 48, pp. 1486–1489, July 1993.
[16] G. H. Vineyard, "Frequency factors and isotope effects in solid state rate processes," *J. Phys. Chem. Solids,* vol. 3, no. 1, pp. 121–127, 1957.
[17] D. Maroudas and R. A. Brown, "Calculation of thermodynamic and transport properties of intrinsic point defects in silicon," *Phys. Rev. B,* vol. 47, no. 23, pp. 15562–15577, 1993.
[18] G. D. Watkins, "Intrinsic point defects in semiconductors," in *Electronic Structure and Properties of Semiconductors (Materials Science and Technology 4),* W. Schröter, Ed. Weinhein, Germany: VCH, 1991, ch. 3, pp. 105–141.
[19] Y. Bar-Yam and J. Joannopoulos, "Microscopic theory of low and high temperature dynamics of intrinsic defects in silicon," in *Proc. 13th Int. Conf. Defects in Semiconduct.,* L. C. Kimerling and J. M. Parsey, Jr., Eds. Warrendale, PA: Metall. Soc. AIME, 1985, pp. 261–267.
[20] S. Tian, "Monte Carlo simulation of ion implantation damage process in silicon: Arsenic, phosphorus, silicon, BF_2, and boron implants," Ph.D. thesis, Univ. Texas, Austin, May 1997.
[21] N. E. B. Cowern, G. F. A. van de Walle, P. C. Zalm, and D. J. Oostra, "Reactions of point defects and dopant atoms in silicon," *Phys. Rev. Lett.,* vol. 69, pp. 116–119, 1992.
[22] F. L. Vook and H. J. Stein, "Relation of neutron to ion damage annealing in Si and Ge," *Radiat. Eff.,* vol. 2, pp. 23–30, 1969.
[23] L. A. Christel, J. F. Gibbons, and T. W. Sigmon, "Displacement criterion for amorphization of silicon during ion implantation," *J. Appl. Phys.,* vol. 52, pp. 7143–7146, Dec. 1981.
[24] S. Prussin, D. I. Margolese, and R. N. Tauber, "Formation of amorphous layers by ion implantation," *J. Appl. Phys.,* vol. 57, pp. 180–185, Jan. 1985.
[25] D. K. Brice, "Ion implantation depth distributions: Energy deposition into atomic processes and ion locations," *Appl. Phys. Lett.,* vol. 16, pp. 103–106, Feb. 1970.
[26] J. Zhu, L. Yang, C. Mailhiot, T. Diaz de la Rubia, and G. H. Gilmer, "*Ab initio* pseudopotential calculations of point defects and boron impurity in silicon," *Nucl. Instrum. Methods Phys. Res. B,* vol. 102, pp. 29–32, 1995.
[27] M. Posselt, "CRYSTAL-TRIM and its application to investigations on channeling effects during ion implantation," *Radiation Effects and Defects in Solids,* vols. 130/131, pp. 87–119, 1994.
[28] S.-H. Yang, S. J. Morris, S. Tian, K. B. Parab, and A. F. Tasch, "Monte Carlo simulation of arsenic ion implantation in (100) single-crystal silicon," *IEEE Trans. Semiconduct. Manufact.,* vol. 9, pp. 49–58, Feb. 1996.
[29] M. Jaraíz, G. H. Gilmer, J. M. Poate, and T. D. de la Rubia, "Atomistic calculations of ion implantation in Si: Point defect and transient enhanced diffusion phenomena," *Appl. Phys. Lett.,* vol. 68, pp. 409–411, Jan. 1996.
[30] S. Tian, "Physical basis of Monte Carlo simulation of ion implantation damage in silicon," Master's thesis, Univ. Texas, Austin, Dec. 1994.
[31] J. R. Beeler, *Radiation Effects Computer Experiments.* Amsterdam/New York: North-Holland, 1983.
[32] H. L. Heinisch, "Defect production in simulated cascades: Cascade quenching and short-term annealing," *J. Nucl. Mater.,* vol. 117, pp. 46–54, 1983.
[33] M. Posselt, "Dynamic simulation of damage accumulation during implantation of BF_2^+ molecular ions into crystalline silicon," *Nucl. Instrum. Methods Phys. Res. B,* vol. 102, pp. 167–172, 1995.
[34] S. Tian, S. J. Morris, B. Obradovic, M. F. Morris, G. Wang, G. Balamurugan, A. F. Tasch, and C. Snell, *UT-MARLOWE Ver. 4.0.,* Univ. Texas, Austin, Mar. 1997.
[35] S. Tian, S. J. Morris, M. Morris, B. Obradovic, and A. F. Tasch, "Monte Carlo simulation of ion implantation damage process in silicon," in *IEDM Tech. Dig.,* 1996, pp. 713–716.
[36] L. C. Feldman, J. W. Mayer, and S. T. Picraux, *Materials Analysis by Ion Channeling: Submicron Crystallography.* New York: Academic, 1982.
[37] R. E. Hummel, W. Xi, P. H. Holloway, and K. A. Jones, "Optical investigations of ion implant at damage in silicon," *J. Appl. Phys.,* vol. 63, pp. 2591–2594, Apr. 1988.
[38] F. F. Morehead, B. L. Crowder, and R. S. Title, "Formation of amorphous silicon by ion bombardment as a function of ion, temperature, and dose," *J. Appl. Phys.,* vol. 43, pp. 1112–1118, Mar. 1972.
[39] P. Gupta, C. Park, K. Klein, S.-H. Yang, S. Morris, V. Do, and A. F. Tasch, "The detailed variation of boron and fluorine profiles with tilt and rotation angles for BF_2^+ ion implantation in (100) silicon," in *Proc. Mater. Res. Soc. Symp.,* 1992, vol. 235, pp. 203–209.
[40] R. Simonton, J. Shi, T. Boden, P. Mailot, and L. Larson, "Flux dependence of amorphous layer formation and damage annealing in room temperature implantation of boron into silicon," in *Proc. Mater. Res. Soc. Symp.,* 1994, vol. 316, pp. 153–157.

Shiyang Tian (M'97) received the B.S. degree in physics from Shandong University, Jinan, China, in 1987, and the M.S. and Ph.D. degrees in electrical engineering from The University of Texas, Austin, in 1994 and 1997, respectively.

Upon graduation, he joined Avant! TCAD Business Unit, Fremont, CA, where he has worked in the development of the advanced process models for TSUPREM-4. His research interests include semiconductor process and device modeling. He has authored or coauthored more than 35 publications in journals and conference proceedings.

Dr. Tian is a Member of the Materials Research Society.

Michael F. Morris received the B.A. degree in physics from Rice University, Houston, TX, in May 1990, the Ph.D. degree in physics from Oklahoma State University, Stillwater, in May 1995, and the M.S. degree in electrical engineering from The University of Texas, Austin, in December 1997.

In January 1998, he joined the Predictive Engineering Labs, Motorola, Inc., Mesa, AZ.

Steven J. Morris received the B.S., M.S., and Ph.D. degrees in electrical engineering from The University of Texas, Austin, in 1992, 1994, and 1997, respectively. His graduate work involved physically-based implant modeling and the application of ion implant simulation for process optimization and control.

In July 1997, he joined Intel Corporation, where he has been working in the TCAD Department on Process Simulation.

Dr. Morris was awarded a SRC Fellowship in 1992 and an Intel Foundation Robert Noyce Memorial Fellowship in 1995.

Borna Obradovic was born on May 2, 1970, in Zagreb, Croatia. He received the B.A. degree in physics in 1993, and the M.S.E. in electrical engineering in 1996, both from The University of Texas, Austin. He is currently pursuing the Ph.D. degree in electrical engineering at the University of Texas, under the supervision of Prof. Al Tasch. His current research interests include Monte Carlo simulation of transport in complex structures, as well as other aspects of TCAD, and microelectronics in general.

Geng Wang received the B.S. degree in physics from Peking University, China, in 1995, and the M.S. degree in electrical engineering from The University of Texas, Austin, in 1997, where he is pursuing the Ph.D. degree. His current research interests include ion implant induced damage modeling and computational efficiency improvement techniques.

Al F. Tasch (M'77–SM'80–F'84), for a photograph and biography, see p. 186 of the January 1998 issue of this TRANSACTIONS.

Charles M. Snell received the B.S. degree in physics from Vanderbilt University, Nashville, TN, in 1967 and the M.S. degree in astrophysics from the University of Arizona, Tucson, in 1969.

He served with the Corps of Engineers Waterways Experiment Station from 1970 to 1974, and was a Staff Member at Lawrence Livermore National Laboratory from 1974 to 1978. Since 1978, he has been with Los Alamos National Laboratory, Los Alamos, NM, and is currently a Staff Member of the Transport Methods Group. His research areas have included stellar photometry, solar system physics, dynamics of planetary cratering, and the use of computer codes to simulate and better understand complex physical phenomena. His current research interests include modeling of ion implantation with binary collision and molecular dynamics methods, and electron beam interaction with rarefied plasmas.